

Active Edge Sites Engineering in Nickel Cobalt Selenide Solid Solutions for Highly Efficient Hydrogen Evolution

Chuan Xia, Hanfeng Liang, Jiajie Zhu, Udo Schwingenschlöggl, and Husam N. Alshareef*

An effective multifaceted strategy is demonstrated to increase active edge site concentration in $\text{Ni}_{0.33}\text{Co}_{0.67}\text{Se}_2$ solid solutions prepared by in situ selenization process of nickel cobalt precursor. The simultaneous control of surface, phase, and morphology result in as-prepared ternary solid solution with extremely high electrochemically active surface area ($C_{dl} = 197 \text{ mF cm}^{-2}$), suggesting significant exposure of active sites in this ternary compound. Coupled with metallic-like electrical conductivity and lower free energy for atomic hydrogen adsorption in $\text{Ni}_{0.33}\text{Co}_{0.67}\text{Se}_2$, identified by temperature-dependent conductivities and density functional theory calculations, the authors have achieved unprecedented fast hydrogen evolution kinetics, approaching that of Pt. Specifically, the $\text{Ni}_{0.33}\text{Co}_{0.67}\text{Se}_2$ solid solutions show a low overpotential of 65 mV at -10 mV cm^{-2} , with onset potential of mere 18 mV, an impressive small Tafel slope of 35 mV dec^{-1} , and a large exchange current density of $184 \mu\text{A cm}^{-2}$ in acidic electrolyte. Further, it is shown that the as-prepared $\text{Ni}_{0.33}\text{Co}_{0.67}\text{Se}_2$ solid solution not only works very well in acidic electrolyte but also delivers exceptional hydrogen evolution reaction (HER) performance in alkaline media. The outstanding HER performance makes this solid solution a promising candidate for mass hydrogen production.

cost-efficient HER catalysts that are based on earth-abundant materials is critical for the future of the hydrogen economy.

Recently, first-row-transition-metal dichalcogenides have been proposed to replace the state-of-the-art Pt group metals, due to their abundance and high catalytic activity toward HER. Especially, metallic CoX_2 ($X = \text{S}, \text{Se}$) with low overpotential, small Tafel slope, and large exchange current has been identified as a promising candidate for HER.^[3–7] For example, the Dai's group and Xie's group showed through theoretical calculations and experimental studies that, similar to the MoS_2 -type materials, the chalcogenide atoms at the edges of CoX_2 catalysts are HER active sites.^[8,9] Furthermore, He and co-workers demonstrated that the edge Se atoms are intrinsic active sites in NiSe_2 electrocatalyst for HER applications.^[10] These findings suggest that maximizing the number of exposed edge sites is a prerequisite to achieving optimal CoX_2 -based HER electrocatalyst

performance. Hence, a series of techniques were reported to further enhance the HER activity of CoX_2 -based materials by regulating the active sites on the atomic scale. For instance, Jin's group reported that ternary CoPS can provide a catalytic overpotential of 48 mV at 10 mA cm^{-2} and an exchange current density of $984 \mu\text{A cm}^{-2}$, superior to binary CoS_2 . They found that the introduction of phosphorus into CoS_2 lattice can create more HER active sites and lower the chemisorption energy of atomic hydrogen to the active sites on the electrocatalyst surface.^[11] Zhang et al. showed that a phase engineering process can be used to produce more edge sites in CoSe_2 catalyst. Specifically, polymorphic (coexisting cubic and orthorhombic) phases of CoSe_2 were achieved by temperature-controlled calcining of amorphous CoSe_x . They pointed out that the grain boundaries between the two different phases would unfold and create new HER active sites, thus further improving the HER activity of CoSe_2 .^[12] Yu et al. demonstrated that higher catalytic performance could be obtained via turning bulk CoSe_2 into ultrathin nanosheet, resulting from the significantly enhanced surface-to-volume ratio and from the vacancy rich surfaces.^[2,13] The exfoliated single-unit-cell CoSe_2 was also proved as a promising candidate for water splitting applications.^[1] In another approach, Xie et al. showed that the Mn-doped CoSe_2 exhibits additional active edge sites and lower kinetic energy barrier for H–H formation compared with pristine CoSe_2 .^[9] While much

1. Introduction

Hydrogen is a sustainable and clean alternative fuel which can replace conventional energy carriers, especially the rapidly diminishing fossil fuels. To date, unfortunately, over 90% of hydrogen is obtained from fossil fuel reformation, a costly process with harmful environmental impact.^[1] Electrochemical water splitting ($2\text{H}_2\text{O} \rightarrow 2\text{H}_2 + \text{O}_2$) offers an alternate promising and environmental-friendly pathway to produce hydrogen at low cost.^[2] However, the mass production of hydrogen from water splitting requires efficient and earth-abundant electrocatalysts for the hydrogen evolution reaction (HER). While platinum (Pt) and its alloys are the benchmark catalysts for HER, the prohibitive cost and scarcity of Pt precludes its adoption for widespread commercial use. Therefore, the search of robust and

C. Xia, Dr. H. Liang, Dr. J. Zhu,
Prof. U. Schwingenschlöggl, Prof. H. N. Alshareef
Materials Science and Engineering
King Abdullah University of Science
and Technology, (KAUST)
Thuwal 23955-6900, Saudi Arabia
E-mail: husam.alshareef@kaust.edu.sa



DOI: 10.1002/aenm.201602089

effort has been done to improve the HER performance of CoSe_2 , the efficiency of mass hydrogen evolution is still not satisfactory. Therefore, the development of efficient CoSe_2 -based HER electrocatalyst with abundant edge sites using simple and cost-efficient routes is still a considerable challenge.

An alternative strategy to increase the number of active sites in CoSe_2 -based HER electrocatalysts is based on introducing Ni-dopant into CoSe_2 to create nanostructured, polymorphic $(\text{Ni}, \text{Co})\text{Se}_2$ solid solutions. To date, there are scattered reports on preparation of Ni-doped CoSe_2 to improve its HER performance, but they suffer from either crystal phase-separation (mixed NiSe_2 and CoSe_2 instead of CoSe_2 -type ternary solid solution) or limited active sites exposure.^[14,15] Hence, although the nanostructured nickel cobalt selenide solid solutions are not well studied, in reality there are multiple scientific arguments that favor this approach. (1) Our density functional theory calculations show that the incorporation of Ni lowers the free energy for atomic hydrogen adsorption on edge Se sites of CoSe_2 (Figure S1, Supporting Information), meaning that potentially higher intrinsic HER activity can be achieved using nickel cobalt selenide solid solutions. (2) Previous reports show that the introduction of nickel cations into cobalt selenides will further increase its electrical conductivity.^[16] The higher conductivity of nickel cobalt selenide makes it more appealing for HER applications due to improved electron transfer. (3) The polymorphic (coexistence of orthorhombic and cubic structures) nature of nickel cobalt selenide increases edge active site concentration on the surface, which is highly desirable for high-performance HER catalyst.^[17,18] (4) Introducing heterogeneous spin states, by the Ni atoms with similar atomic radius and electron configuration into the CoSe_2 crystal lattice, could generate a subtle distortion in the lattice. This distortion may originate from: (i) the localized Coulomb interaction around the Ni atoms arising from the introduction of the incoordinated electron spins; (ii) the mismatch in the degree of Jahn–Teller distortion between the Ni–Se and Co–Se coordination octahedra (Ni^{2+} , $t_{2g}^6 e_g^2$, no Jahn–Teller effect; Co^{2+} , $t_{2g}^6 e_g^1$, strong Jahn–Teller effect).^[9,19]

In light of these potential benefits, we report a very simple one-step approach for phase, surface, and morphology engineered nickel cobalt selenide solid solution, namely $\text{Ni}_{0.33}\text{Co}_{0.67}\text{Se}_2$ for HER electrocatalyst application. The obtained $\text{Ni}_{0.33}\text{Co}_{0.67}\text{Se}_2$ with mixed cubic and orthorhombic phases shows a unique morphology of interconnected nanowire arrays, where the nanowires are composed of self-assembled nanometer-scale $\text{Ni}_{0.33}\text{Co}_{0.67}\text{Se}_2$ nanosheets. Importantly, the as-prepared $\text{Ni}_{0.33}\text{Co}_{0.67}\text{Se}_2$ shows an extremely high electrochemically active surface area (ECSA) ($C_{dl} = 197 \text{ mF cm}^{-2}$), which is at least twofold higher than that reported for advanced HER catalysts. When evaluated as HER electrocatalyst, $\text{Ni}_{0.33}\text{Co}_{0.67}\text{Se}_2$ solid solution exhibits much higher catalytic activity and better stability than pure CoSe_2 . The as-prepared $\text{Ni}_{0.33}\text{Co}_{0.67}\text{Se}_2$ achieves a geometrical catalytic current density of -10 mA cm^{-2} at overpotential as low as 65 mV with a low Tafel slope of 35 mV dec^{-1} , approaching the performance of Pt. Impressively, there is no performance loss of as-obtained $\text{Ni}_{0.33}\text{Co}_{0.67}\text{Se}_2$ architecture after continues 24 h electrolysis. What is more, we further show that the $\text{Ni}_{0.33}\text{Co}_{0.67}\text{Se}_2$ catalyst not only works very well in acidic electrolyte but also delivers exceptional HER performance in

alkaline media. The outstanding HER performance makes the presented sample a promising candidate for hydrogen production applications.

2. Results and Discussion

We synthesized $\text{Ni}_{0.33}\text{Co}_{0.67}\text{Se}_2$ nanoarchitecture using a simple solvothermal method by in situ selenization of nickel-cobalt-precursor $[(\text{Ni}, \text{Co})(\text{CO}_3)_{0.5}(\text{OH}) \cdot 0.11\text{H}_2\text{O}]$ nanowire arrays in ethylenediamine (en) solution (see details in the Experimental Section). It is known that electron transfer between neighboring catalyst particles is poor during the HER process in conventional binder-involved electrocatalysts.^[9] Thus, to circumvent this disadvantage, $(\text{Ni}, \text{Co})(\text{CO}_3)_{0.5}(\text{OH}) \cdot 0.11\text{H}_2\text{O}$ nanoarrays grown on carbon fiber paper (CFP) were used as precursor (Figure S2, Supporting Information) to obtain the 3D, binder-free selenide catalysts. Moreover, the direct growth process lowers the contact resistance between the catalyst and substrate, hence minimizing the Ohmic losses in the system during the electrocatalysis.^[20] The CFP was used here as current collector due to its low-cost, chemically inert nature, high conductivity, and negligible HER activity.^[16,21–24] To investigate the structural information of the selenized products, we first employed X-ray diffraction (XRD) measurements. The θ – 2θ XRD pattern (Figure 1A) supports the formation of CoSe_2 -type $\text{Ni}_{0.33}\text{Co}_{0.67}\text{Se}_2$ solid solution with mixed cubic (JCPDS Card 88-1712) and orthorhombic (JCPDS Card 53-0449) crystal structures. The enlarged XRD pattern (Figure 1B) shows that all diffraction peaks shift to lower angles compared to those of CoSe_2 , which is caused by the incorporation of Ni into CoSe_2 lattice. Inductively coupled plasma optical emission spectroscopy (ICP-OES) analysis revealed that the Ni/Co/Se ratio of the product is very close to 1:2:6, giving a stoichiometric formula of $\text{Ni}_{0.33}\text{Co}_{0.67}\text{Se}_2$. Interestingly, compared to the as-obtained $\text{Ni}_{0.33}\text{Co}_{0.67}\text{Se}_2$, all the XRD diffraction peaks of the argon annealed sample split into two subpeaks that can be respectively identified as CoSe_2 and NiSe_2 (Figure S3, Supporting Information). This phase evolution induced by thermal annealing strongly supports the formation of nickel cobalt selenide solid solution (with single composition $\text{Ni}_{0.33}\text{Co}_{0.67}\text{Se}_2$) but not two separate phases (CoSe_2 with NiSe_2) during the in situ selenization process. We further measured the magnetic field dependence of magnetization (M – H) curves of pristine CoSe_2 and $\text{Ni}_{0.33}\text{Co}_{0.67}\text{Se}_2$ solid solution at room temperature to verify the incorporation of heterogeneous spin state, namely Ni, into CoSe_2 lattice. As shown in Figure 1C, the pure CoSe_2 shows negligible ferromagnetic feature by the fact that the M – H hysteresis loop is inconspicuous, whereas that of $\text{Ni}_{0.33}\text{Co}_{0.67}\text{Se}_2$ is obvious.^[25–27] Moreover, the coercivity of $\text{Ni}_{0.33}\text{Co}_{0.67}\text{Se}_2$ is about sixfold higher than that of CoSe_2 (inset of Figure 1C). Such significant difference in magnetic behavior further confirms that we have successfully formed the $\text{Ni}_{0.33}\text{Co}_{0.67}\text{Se}_2$ phase. As we mentioned earlier, it has been demonstrated that subtle atomic distortions may occur after the introduction of heterogeneous spin states.^[9] As illustrated in Scheme 1, pyrite-type CoSe_2 (cubic structure) involves corner sharing of distorted Co–Se octahedra, whereas in marcasite-type CoSe_2 (orthorhombic structure), share edges and form chains of linked octahedra.^[28]

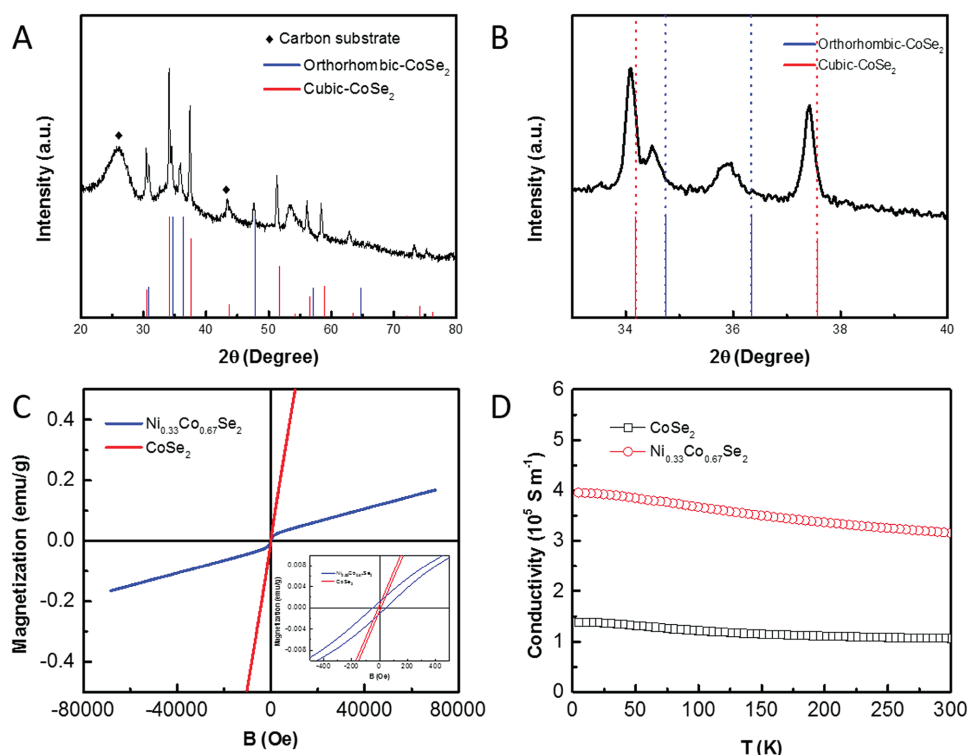
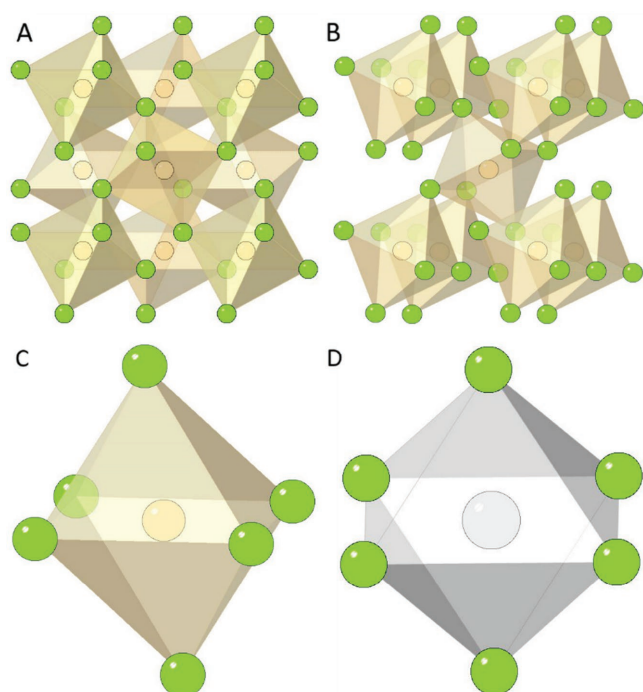


Figure 1. A,B) Representative XRD pattern for as-prepared $\text{Ni}_{0.33}\text{Co}_{0.67}\text{Se}_2$ nanowire arrays on CFP. C) The magnetic field dependence of magnetization curve of as-prepared selenides. D) Temperature dependence of conductivity of the $\text{Ni}_{0.33}\text{Co}_{0.67}\text{Se}_2$ and CoSe_2 pellets compressed from ternary selenide nanopowders.



Scheme 1. Crystal structures of A) cubic and B) orthorhombic CoSe_2 . C) The distorted Co-Se octahedral building block in CoSe_2 . D) The Ni-Se octahedral building block in NiSe_2 which shows a perfect octahedral configuration. Green: Se atom; Yellow: Co atom; Gray: Ni atom.

Thus, the distorted Co-Se octahedra are normally the basic building units for CoSe_2 crystal. Undoubtedly, the mismatch in the degree of Jahn–Teller distortion between Co-Se octahedra (strong Jahn–Teller effect; distorted octahedra building block) and Ni-Se octahedra (no Jahn–Teller effect; perfect octahedra building unit) yields more variations in the atomic arrangement during the formation of $\text{Ni}_{0.33}\text{Co}_{0.67}\text{Se}_2$ solid solution, creating point defects and defect clusters which can act as active sites for HER.^[9] Moreover, the coexistence of cubic and orthorhombic systems can lead to the creation of more grain boundaries, augmenting the number of marginal chalcogen atom active sites. These features ensure the abundant active site exposure in our $\text{Ni}_{0.33}\text{Co}_{0.67}\text{Se}_2$ catalyst. As another important parameter for HER application, the electrical transport properties of the synthetic selenides were evaluated experimentally from the temperature dependence of conductivity. As shown in Figure 1D, the conductivity of the selenides decreases linearly with temperature from 2 to 300 K, indicating their metallic nature. Importantly, the room-temperature electrical conductivity of $\text{Ni}_{0.33}\text{Co}_{0.67}\text{Se}_2$ is about threefold higher than that of pure CoSe_2 , suggesting the $\text{Ni}_{0.33}\text{Co}_{0.67}\text{Se}_2$ is even more conductive after Ni incorporation.^[16] Hence, apparently, $\text{Ni}_{0.33}\text{Co}_{0.67}\text{Se}_2$ exhibits clear advantages over pristine CoSe_2 for HER application.

The morphology of as-obtained $\text{Ni}_{0.33}\text{Co}_{0.67}\text{Se}_2$ was investigated by scanning electron microscopy (SEM) and transmission electron microscopy (TEM). Figure 2A shows a low-magnification SEM image of $\text{Ni}_{0.33}\text{Co}_{0.67}\text{Se}_2$ /CFP, indicating the entire

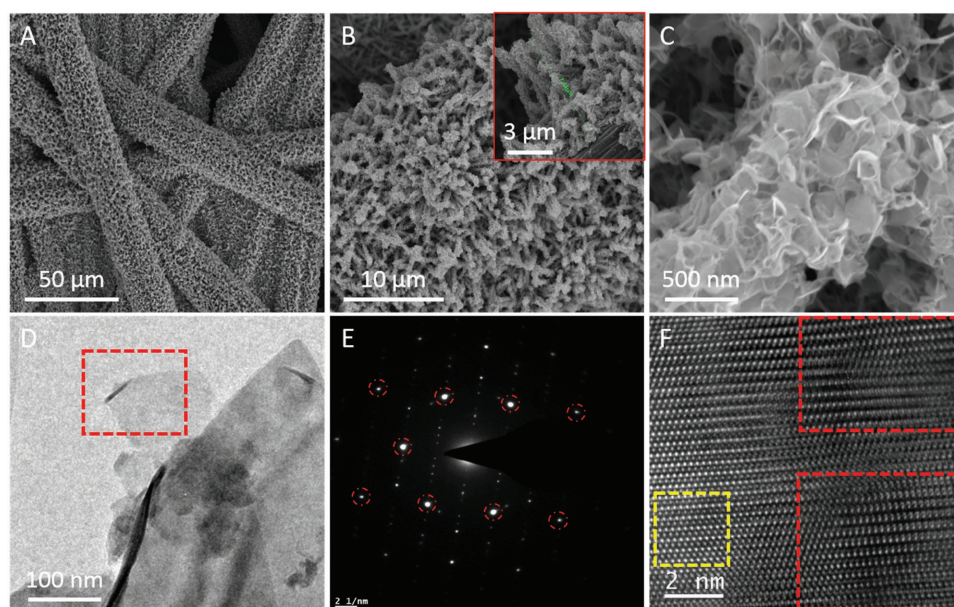


Figure 2. A–C) Typical SEM images for as-prepared $\text{Ni}_{0.33}\text{Co}_{0.67}\text{Se}_2$ on CFP, showing ultrathin nanosheet assembled nanowire architecture. D) The TEM image of an individual $\text{Ni}_{0.33}\text{Co}_{0.67}\text{Se}_2$ nanosheet. E) The corresponding SAED pattern of $\text{Ni}_{0.33}\text{Co}_{0.67}\text{Se}_2$ nanosheet taken from the area marked in panel (D). F) Representative HRTEM image of $\text{Ni}_{0.33}\text{Co}_{0.67}\text{Se}_2$ nanosheet.

surface of our CFP was uniformly covered with interconnected $\text{Ni}_{0.33}\text{Co}_{0.67}\text{Se}_2$ nanowires. The close-up images (Figure 2B,C) reveal that the nanowires with lengths of $\approx 7.5 \mu\text{m}$ are actually composed of $\text{Ni}_{0.33}\text{Co}_{0.67}\text{Se}_2$ nanosheets. Atomic force microscopy (AFM) result (Figure S4, Supporting Information) shows that these nanosheets are ultrathin with thicknesses of 1–5 nm (as thin as few CoSe_2 slab). It has been demonstrated and well accepted that the ultrathin sheet-like electrocatalysts are able to provide better catalytic performance than their bulk counterparts, resulting from the increased surface-to-volume ratio and enhanced active site concentration on their basal surface.^[29–31] While the conventional liquid exfoliation method has been widely applied to produce ultrathin (or monolayer) materials, the high-cost, complicated experimental operation, and low throughput limit its large scale application in water splitting. Thus, the one-step in situ selenization method devolved here offers clear advantages compared to the postexfoliation routes often use in the preparation of ultrathin nanosheets. Likewise, the fabrication process of binder-free $\text{Ni}_{0.33}\text{Co}_{0.67}\text{Se}_2$ catalyst through conversion of dense $(\text{Ni},\text{Co})(\text{CO}_3)_{0.5}(\text{OH}) \cdot 0.11\text{H}_2\text{O}$ nanoarray precursor also offers the possibility to achieve high geometrical mass loading of the catalyst, thereby resulting in a relatively higher catalytic performance. Figure 2D displays the TEM image of the $\text{Ni}_{0.33}\text{Co}_{0.67}\text{Se}_2$ product, which again verifies the ultrathin feature of the nanosheets. As presented in Figure 2E, the selected area electron diffraction (SAED) pattern from an individual $\text{Ni}_{0.33}\text{Co}_{0.67}\text{Se}_2$ nanosheet (marked area in Figure 2D) shows two sets of single-crystal patterns. Notably, the red-circled diffraction spots are attributed to the cubic phase whereas the others are ascribed to the orthorhombic phase. Hence, the SAED patterns confirm the coexisting of mixed cubic and orthorhombic $\text{Ni}_{0.33}\text{Co}_{0.67}\text{Se}_2$ phases, in agreement with XRD result. To visually demonstrate the surface disordered

atomic arrangement in $\text{Ni}_{0.33}\text{Co}_{0.67}\text{Se}_2$, we conducted high-resolution TEM (HRTEM) analysis. As shown in Figure 2E, the regular (yellow-marked) and twisted (red-marked) atomic arrangement are both observed on the basal surface of the $\text{Ni}_{0.33}\text{Co}_{0.67}\text{Se}_2$ nanosheet, which clearly demonstrates the formation of surface distorted samples. This enhanced degree of surface disorder is believed to increase the number of active edge sites, which is beneficial to electrocatalysis.^[32–34] Given the high conductivity and the abundant active edge sites as demonstrated above, one can expect that the $\text{Ni}_{0.33}\text{Co}_{0.67}\text{Se}_2$ solid solution would have superior catalytic performance toward the HER.

On the basis of our experimental results and previous literature reports, we propose the following mechanism for the formation of the hierarchical $\text{Ni}_{0.33}\text{Co}_{0.67}\text{Se}_2$ solid solution nanostructures: (1) The $(\text{Ni},\text{Co})(\text{CO}_3)_{0.5}(\text{OH}) \cdot 0.11\text{H}_2\text{O}$ nanowire precursor serves as a template for the selenide growth.^[16] (2) Ethylenediamine, a bidentate compound, was selected as solvent due to its strong N-chelation ability.^[35] It can react with the NiCo-precursor at the solid–liquid interface to form relatively stable NiCo-en complexes and simultaneously release CO_3^{2-} , OH^- , and H_2O . Then, as previously proved, the disproportionation of Se occurs in the presence of CO_3^{2-} or OH^- under solvothermal conditions to generate Se_2^{2-} ions (e.g., $3\text{CO}_3^{2-} + 6\text{Se} \rightarrow 2\text{Se}_2^{2-} + \text{Se}_2\text{O}_3^{2-} + 3\text{CO}_2$).^[36,37] In addition, the nucleophilic attack by ethylenediamine can also activate elemental selenium to form Se_2^{2-} ions.^[38] (3) With temperature increase, the stability of the NiCo-en complex is expected to decrease. Then, these complexes decompose and coordinate with Se_2^{2-} to produce $\text{Ni}_{0.33}\text{Co}_{0.67}\text{Se}_2$ nuclei. (4) Next, the protonated en molecules (reacting with H_2O at high-temperature) with positively charged ammonium ions are incorporated into $\text{Ni}_{0.33}\text{Co}_{0.67}\text{Se}_2$ slab by coordination with Se atoms.^[39] Afterward, protonated-en and virgin-en with a linear configuration

acts, respectively, as a template and surface passive agent to induce the anisotropic growth of ultrathin $\text{Ni}_{0.33}\text{Co}_{0.67}\text{Se}_2$ nanosheet, which is very analogous to the so-called solvent coordination molecular templating mechanism.^[39,40] (5) The formed $\text{Ni}_{0.33}\text{Co}_{0.67}\text{Se}_2$ nanosheets are attached on the surface of remained $(\text{Ni},\text{Co})(\text{CO}_3)_{0.5}(\text{OH}) \cdot 0.11\text{H}_2\text{O}$ nanowire. Thanks to the gradual “etching” of the $(\text{Ni},\text{Co})(\text{CO}_3)_{0.5}(\text{OH}) \cdot 0.11\text{H}_2\text{O}$ nanowire surface, such a unique nanosheet self-assembled nanowire morphology is finally generated.

To assess the HER electrocatalytic activity of $\text{Ni}_{0.33}\text{Co}_{0.67}\text{Se}_2$ solid solution, the corresponding polarization curves in 0.5 M H_2 -saturated H_2SO_4 were recorded at a scan rate of 2.0 mV s^{-1} . The pristine CoSe_2 (with similar morphology and phase compared to $\text{Ni}_{0.33}\text{Co}_{0.67}\text{Se}_2$) and Pt wire were also examined for comparison. The potentials were measured versus saturated calomel electrode (SCE) for all experimental tests but are reported here versus reversible hydrogen electrode (RHE) (see details in the Experimental Section). **Figure 3A** shows that the $\text{Ni}_{0.33}\text{Co}_{0.67}\text{Se}_2$ electrodes achieved the geometrical current density (J) of -10 mA cm^{-2} at a very low overpotential (η) of 65 mV, with an onset η of 18 mV. By contrast, the pristine CoSe_2 needs 109 mV to deliver a significant H_2 evolution ($J = -10 \text{ mA cm}^{-2}$), which is 1.7-fold higher than that of $\text{Ni}_{0.33}\text{Co}_{0.67}\text{Se}_2$. In addition, $\text{Ni}_{0.33}\text{Co}_{0.67}\text{Se}_2$ and CoSe_2 electrodes need η of 94 and 38 mV to drive a current density of -50 mA cm^{-2} , respectively. In comparison, $\text{Ni}_{0.33}\text{Co}_{0.67}\text{Se}_2$ electrode shows much lower catalytic overpotential than previously reported for nickel or cobalt-based catalyst such as CoS_2 (-145 mV for $J = -10 \text{ mA cm}^{-2}$),^[21] CoSe_2

(-180 mV for $J = -10 \text{ mA cm}^{-2}$),^[4] CoP (-67 mV for $J = -10 \text{ mA cm}^{-2}$),^[41] and NiSe_2 (-117 mV for $J = -10 \text{ mA cm}^{-2}$),^[10] clearly showing the outstanding performance of ternary $\text{Ni}_{0.33}\text{Co}_{0.67}\text{Se}_2$ solid solutions. The HER kinetics of our selenide electrodes was evaluated by their corresponding Tafel plots (**Figure 3B**). Our calculations show Tafel slopes of ≈ 35 and $\approx 42 \text{ mV dec}^{-1}$ per decade for $\text{Ni}_{0.33}\text{Co}_{0.67}\text{Se}_2$ and CoSe_2 , respectively, which are close to that of Pt (30 mV dec^{-1}). The decrease of Tafel slope from binary CoSe_2 to ternary $\text{Ni}_{0.33}\text{Co}_{0.67}\text{Se}_2$ further demonstrates the enhancement of the intrinsic HER activity of $\text{Ni}_{0.33}\text{Co}_{0.67}\text{Se}_2$ after Ni incorporation. In fact, the Tafel slope of $\text{Ni}_{0.33}\text{Co}_{0.67}\text{Se}_2$ is either lower than or comparable to all reported noble-metal-free HER catalysts in the literature (Table S1, Supporting Information). Additionally, we estimated the resistances of $\text{Ni}_{0.33}\text{Co}_{0.67}\text{Se}_2$ and CoSe_2 electrodes using electrical impedance spectroscopy (EIS). The $\text{Ni}_{0.33}\text{Co}_{0.67}\text{Se}_2$ exhibited a lower equivalent series resistance (ESR) ($\approx 2.36 \Omega$) and charge transfer resistance (R_{ct}) ($\approx 0.27 \Omega$) than pure CoSe_2 (ESR = $\approx 3.92 \Omega$; R_{ct} = $\approx 0.48 \Omega$) (**Figure S5**, Supporting Information). The lower resistance in ternary $\text{Ni}_{0.33}\text{Co}_{0.67}\text{Se}_2$ electrode leads to more favorable charge transport kinetics, showing another positive feature of nickel incorporation into CoSe_2 (to form in $\text{Ni}_{0.33}\text{Co}_{0.67}\text{Se}_2$). As we know, the value of exchange current densities (J_0) represents the inherent HER activity of the catalyst. In this regards, we extracted the J_0 of our samples by extrapolating the corresponding Tafel slopes.^[11,41] A J_0 of $184 \mu\text{A cm}^{-2}$ was obtained for $\text{Ni}_{0.33}\text{Co}_{0.67}\text{Se}_2$ nanostructure, which surpasses the value of $26.5 \mu\text{A cm}^{-2}$ for CoSe_2 as well as the value of other reported

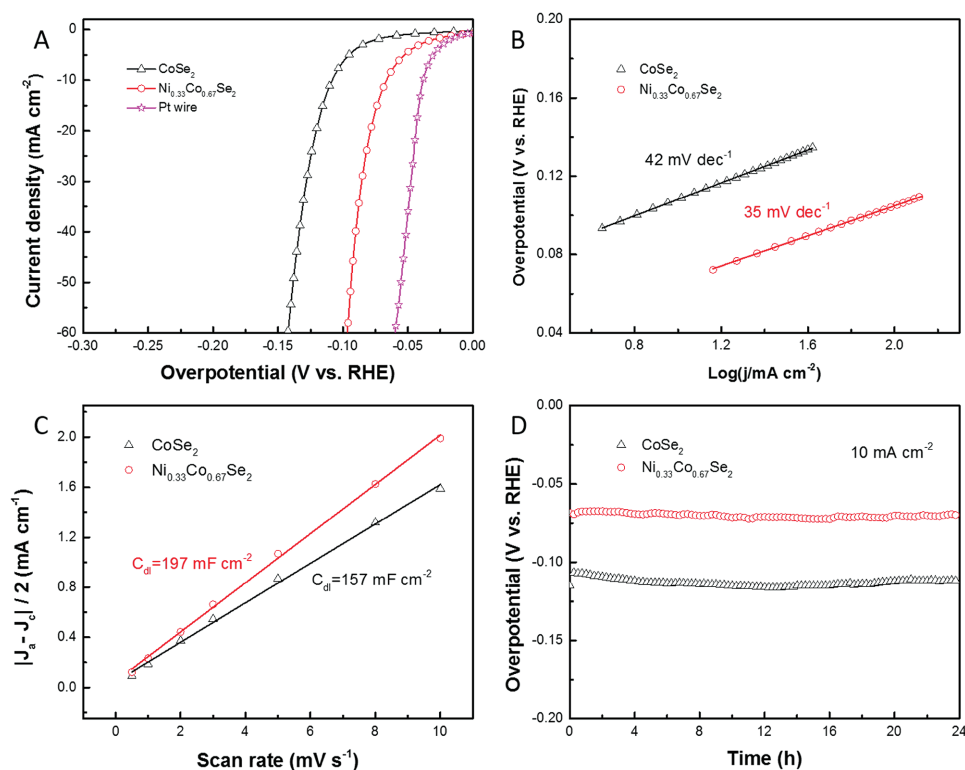


Figure 3. A) The iR -corrected polarization curves of $\text{Ni}_{0.33}\text{Co}_{0.67}\text{Se}_2$, CoSe_2 , and Pt wire in H_2 -saturated 0.5 M H_2SO_4 solution and B) the corresponding Tafel plots. C) Plots showing the extraction of the double-layer capacitance for all studied samples. D) Long-term stability measurements at $j = 10 \text{ mA cm}^{-2}$ for as-obtained $\text{Ni}_{0.33}\text{Co}_{0.67}\text{Se}_2$ and CoSe_2 .

advanced HER catalysts (Table S1, Supporting Information). The approximately sevenfold higher exchange current density explains the better HER catalytic performance of ternary $\text{Ni}_{0.33}\text{Co}_{0.67}\text{Se}_2$. Undoubtedly, this enhancement in inherent HER activity can be attributed to the unique structure, the high conductivity, and abundant active edge sites in the solid solution.

In an attempt to further understand the significant difference in HER catalytic performance between $\text{Ni}_{0.33}\text{Co}_{0.67}\text{Se}_2$ and CoSe_2 , we estimated their relative ECSA. This is done by using cyclic voltammetry measurements and extracting the double-layer capacitance (C_{dl}), which is expected to be linearly proportional to the actual effective active surface area in the catalyst material.^[11,42] As shown in Figure 3C, $\text{Ni}_{0.33}\text{Co}_{0.67}\text{Se}_2$ and CoSe_2 both show extremely high C_{dl} of 197 and 157 mF cm^{-2} , respectively. These exceedingly large C_{dl} numbers clearly indicate very high exposure of the active sites in this material, a result which is consistent with the other positive characteristics discussed earlier. The higher C_{dl} value obtained in the case of $\text{Ni}_{0.33}\text{Co}_{0.67}\text{Se}_2$ (197 mF cm^{-2} vs 157 mF cm^{-2} for CoSe_2) proves the efficacy of our strategy of introducing heterogeneous spin state (Ni) into CoSe_2 lattice to create more atomic active sites and to boost HER performance. Of note, the C_{dl} value of $\text{Ni}_{0.33}\text{Co}_{0.67}\text{Se}_2$ is much higher than that of recently reported high-performance HER catalysts such as exfoliated single-unit-cell thick CoSe_2 nanosheet (41.6 mF cm^{-2}),^[1] exfoliated $\text{Mn}_{0.5}\text{Co}_{0.95}\text{Se}_2$ nanosheet (16.25 mF cm^{-2}),^[9] CoPS nanowire (99.6 mF cm^{-2}),^[11] NiSe_2 nanowall (68.2 mF cm^{-2}),^[43] and ultrathin NiFe-S nanosheet (46.4 mF cm^{-2}).^[44] Such high

C_{dl} values for both $\text{Ni}_{0.33}\text{Co}_{0.67}\text{Se}_2$ and CoSe_2 , which are realized using a simple in situ selenization process, suggest the superiority of our simple solvothermal route compared to other techniques. Therefore, on the basis of this systematic analysis, we believe that the one-step realized surface, phase, and morphology engineering in the $\text{Ni}_{0.33}\text{Co}_{0.67}\text{Se}_2$ leads to such an ideal HER activity (high kinetic metrics, high C_{dl} , and large J_0), making it a competitive alternative to Pt-based HER electrocatalysts.

Apart from the HER catalytic performance, the long-term durability of the catalyst is another pivotal concern for real-world electrolysis. As shown in Figure 3D, the stabilities of as-fabricated catalysts were tested at a constant current density of -10 mA cm^{-2} for 24 h. Noticeably, the overpotential of $\text{Ni}_{0.33}\text{Co}_{0.67}\text{Se}_2$ electrodes remained nearly constant after 24 h of continuous electrolysis. To be specific, the η required to deliver -10 mA cm^{-2} only slightly shifts from 65 to 69 mV after 24 h, showing the good stability in strong-acid conditions. The 24 h cycled $\text{Ni}_{0.33}\text{Co}_{0.67}\text{Se}_2$ samples were further investigated. The XRD pattern (Figure 4A) shows that there is no phase change in the postcatalytic $\text{Ni}_{0.33}\text{Co}_{0.67}\text{Se}_2$, meaning that the coexisting cubic and orthorhombic $\text{Ni}_{0.33}\text{Co}_{0.67}\text{Se}_2$ have survived after vigorous hydrogen evolution. Figure 4B displays the high-resolution X-ray photoelectron spectroscopy (XPS) of Se 3d spectrum of as-prepared $\text{Ni}_{0.33}\text{Co}_{0.67}\text{Se}_2$. The peak fitting analysis reveals that the binding energies of Se $3d_{5/2}$ and $3d_{3/2}$ at 53.8 and 54.5 eV, respectively, are very close to those observed for CoSe_2 and NiSe_2 .^[4,15,16] The XPS analysis of postcatalytic $\text{Ni}_{0.33}\text{Co}_{0.67}\text{Se}_2$ (Figure 4C) shows that the surface Ni-Se/Co-Se

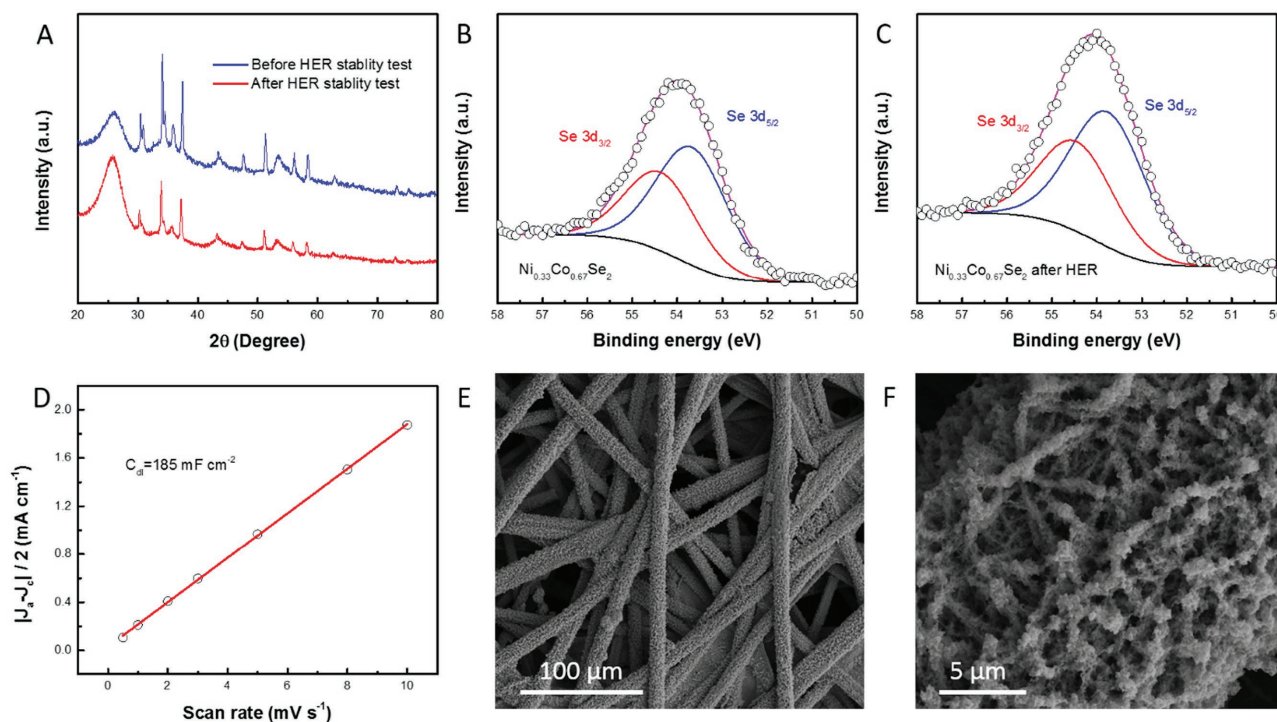


Figure 4. A) The XRD patterns of $\text{Ni}_{0.33}\text{Co}_{0.67}\text{Se}_2$ sample before and after the HER. B,C) The high-resolution XPS spectra of Se 3d of $\text{Ni}_{0.33}\text{Co}_{0.67}\text{Se}_2$ before and after cycling. D) Plot of the double-layer capacitance for postcatalytic $\text{Ni}_{0.33}\text{Co}_{0.67}\text{Se}_2$. E,F) The typical SEM images of $\text{Ni}_{0.33}\text{Co}_{0.67}\text{Se}_2$ /CFP after 24 h electrolysis.

bonds in $\text{Ni}_{0.33}\text{Co}_{0.67}\text{Se}_2$ are not changed after cycling, suggesting the survival of the active edge sites. More indicatively, we tried to compare the C_{dl} of $\text{Ni}_{0.33}\text{Co}_{0.67}\text{Se}_2$ before and after long-term electrolysis (Figure 4D). Encouragingly, the C_{dl} of cycled $\text{Ni}_{0.33}\text{Co}_{0.67}\text{Se}_2$ catalyst (185 mF cm^{-2}) is comparable to that of fresh samples (197 mF cm^{-2}). The ECSA analysis shows that the HER active sites in $\text{Ni}_{0.33}\text{Co}_{0.67}\text{Se}_2$ catalyst are remarkably robust in acidic solution, unequivocally demonstrating its excellent stability. In fact, we observed a very similar morphology (Figure 4E,F) for postcatalytic $\text{Ni}_{0.33}\text{Co}_{0.67}\text{Se}_2$ samples compared to fresh samples. Generally, from our systematic measurements of $\text{Ni}_{0.33}\text{Co}_{0.67}\text{Se}_2$ catalyst, it is fair to conclude here that the as-prepared $\text{Ni}_{0.33}\text{Co}_{0.67}\text{Se}_2$ nanoarrays are very efficient and stable to catalyze mass hydrogen evolution in acidic solution.

As we known, strongly acidic or alkaline solution is always required to minimize the overpotential during electrochemical water splitting process. However, a high-performance HER catalyst at acidic solution may be inactive or even unstable in basic electrolyte and vice versa.^[45,46] An HER catalyst which can efficiently work in wide pH range is desirable for real-world hydrogen production. To further evaluate the potential of $\text{Ni}_{0.33}\text{Co}_{0.67}\text{Se}_2$ nanoarrays for widespread HER applications, we recorded the polarization curve of fresh $\text{Ni}_{0.33}\text{Co}_{0.67}\text{Se}_2$ in 1.0 M H_2 -saturated KOH at a scan rate of 2.0 mV s^{-1} . As shown in Figure 5A, the measured onset overpotential is mere 51 mV and only 106 mV is required to drive apparent hydrogen evolution ($j = -10 \text{ mA cm}^{-2}$). Besides, as exhibited in Figure 5B, the estimated Tafel slope (60 mV dec^{-1}) highlights its promising

HER kinetic in alkaline electrolyte. Ascribed to the unique structure of $\text{Ni}_{0.33}\text{Co}_{0.67}\text{Se}_2$ catalyst, this electrode also presents high C_{dl} (96 mF cm^{-2}) in KOH solution (Figure 5C). Moreover, the extracted J_0 ($143 \mu\text{A cm}^{-2}$) also suggests the inherent HER catalytic activity of $\text{Ni}_{0.33}\text{Co}_{0.67}\text{Se}_2$ in basic electrolyte. It is worthwhile to note that all the estimated catalytic parameters are superior to other reported earth-abundant catalysts in alkaline solution (Table S1, Supporting Information), clearly showing its potential for widespread HER applications. In addition, its excellent durability was further identified by continuous 24 h electrolysis reaction (Figure 5D). All the remarkable features promise the potential of our $\text{Ni}_{0.33}\text{Co}_{0.67}\text{Se}_2$ catalyst for HER applications in both acidic and basic media.

3. Conclusions

In summary, phase, surface, and morphology engineered $\text{Ni}_{0.33}\text{Co}_{0.67}\text{Se}_2$ solid solutions are successfully optimized using a simple in situ selenization process of $(\text{Ni,Co}) (\text{CO}_3)_{0.5}(\text{OH}) \cdot 0.11\text{H}_2\text{O}$ precursor. The simultaneous optimization of multiple factors in a single step results in ternary $\text{Ni}_{0.33}\text{Co}_{0.67}\text{Se}_2$ catalysts with a very large electrochemically active surface area (197 mF cm^{-2}). We further demonstrate that an apparently disordered atomic arrangement in $\text{Ni}_{0.33}\text{Co}_{0.67}\text{Se}_2$ nanosheet can be realized by incorporation of heterogeneous spin states (e.g., Ni into CoSe_2). Moreover, the metal-like electrical conductivity and lower free energy for atomic hydrogen adsorption in $\text{Ni}_{0.33}\text{Co}_{0.67}\text{Se}_2$, identified by temperature-dependent

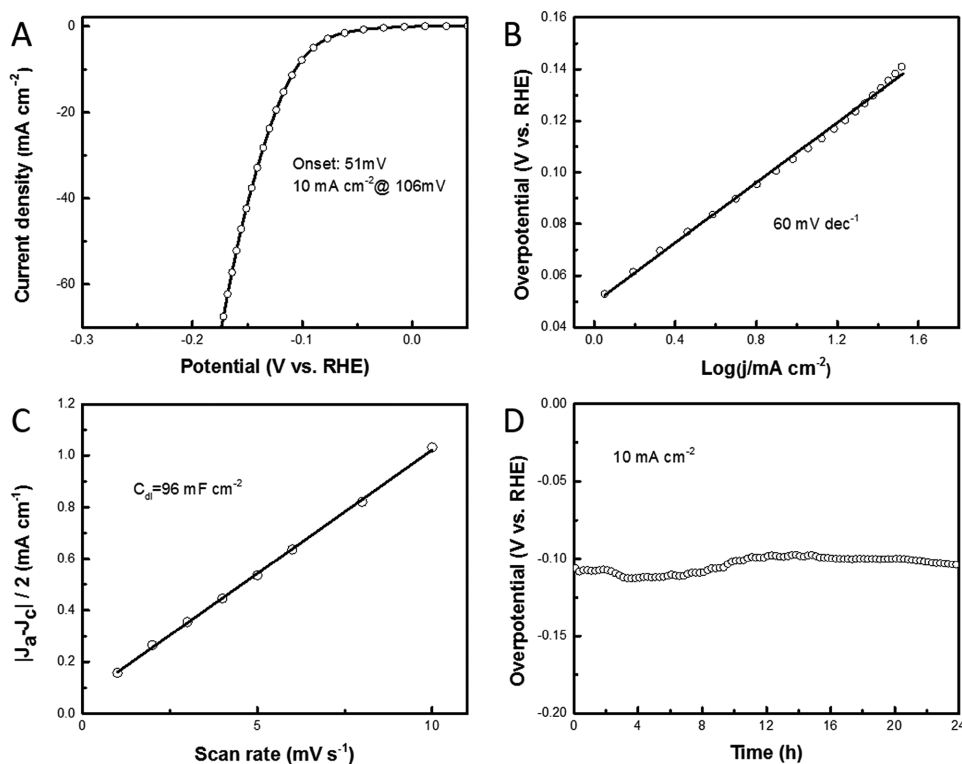


Figure 5. A) The iR -corrected polarization curves of $\text{Ni}_{0.33}\text{Co}_{0.67}\text{Se}_2$ in H_2 -saturated 1.0 M KOH solution and B) the corresponding Tafel plot. C) Estimation of the double-layer capacitance of $\text{Ni}_{0.33}\text{Co}_{0.67}\text{Se}_2$ in basic solution. D) Stability test at the current density of 10 mA cm^{-2} in 1.0 M KOH electrolyte.

conductivities and density functional theory calculations, ensures fast hydrogen evolution kinetics. The as-prepared $\text{Ni}_{0.33}\text{Co}_{0.67}\text{Se}_2$ nanoarrays offer a very promising hydrogen-evolving cathode with high activity and good stability in both strongly acidic and basic electrolytes. This work provides a new and simple avenue toward efficient HER catalyst design.

4. Experimental Section

Cobalt-Precursor and Nickel-Cobalt-Precursor Synthesis: Cobalt-precursor $[\text{Co}(\text{CO}_3)_{0.5}(\text{OH})\cdot 0.11\text{H}_2\text{O}]$ and nickel-cobalt-precursor $[(\text{Ni},\text{Co})(\text{CO}_3)_{0.5}(\text{OH})\cdot 0.11\text{H}_2\text{O}]$ nanowire arrays on CFP were prepared by one-step hydrothermal method as described in refs. [16,47,48].

CoSe₂ and Ni_{0.33}Co_{0.67}Se₂ Synthesis: In a typical procedure, 1 mmol Se powder was first added into 40 mL ethylenediamine solution. Then, this solution was sonicated for 2 h to form a homogeneous solution. Next, one piece of as-prepared precursor (Co-precursor or NiCo-precursor on CFP) and 40 mL of above solution were loaded into a Teflon lined stainless steel autoclave. The autoclave was heated at 180 °C for 12 h and then cooled to room temperature naturally. The final product was washed using ethanol and ultrapure water, and dried in vacuum at 60 °C. The annealed $\text{Ni}_{0.33}\text{Co}_{0.67}\text{Se}_2$ sample was prepared by annealing fresh $\text{Ni}_{0.33}\text{Co}_{0.67}\text{Se}_2$ in argon at 400 °C for 1 h.

Characterization: XRD spectra were collected by a Bruker diffractometer (D8 Advance) with $\text{Cu K}\alpha$ radiation, $\lambda = 1.5406 \text{ \AA}$. XPS was obtained from Kratos AXIS Ultra DLD. The morphology and microstructure of the samples were characterized by SEM (Nova Nano 630, FEI) and TEM (Titan 80–300 kV). AFM images were recorded using a Digital Instrument Multi-Mode AFM with a Nanoscope four controller operating in tapping mode. ICP-OES test was performed on Varian 720-ES. Transport measurements were carried out on a physical property measurement system (PPMS-9, Quantum Design). The authors measured the magnetic properties using a Quantum Design magnetic property measurement system.

Electrochemical Measurements: All Electrochemical tests were carried out at room temperature in three-electrode configurations and recorded using Bio-Logic VMP3. H_2 -saturated 0.5 M H_2SO_4 or 1.0 M KOH was used as electrolyte. The as-prepared CoSe₂ and $\text{Ni}_{0.33}\text{Co}_{0.67}\text{Se}_2$ on CFP were directly used as working electrodes. A graphite rod and a SCE were used as counter electrode and reference electrode, respectively. Before electrochemical measurements, all the samples were first stabilized using a number of potential sweeps. All polarization curves were recorded under a sweep rate of 2.0 mV s^{-1} . EIS was recorded under the following conditions: ac voltage amplitude of 5 mV, frequency ranges from 10^5 to 0.1 Hz, and open circuit. Chronopotentiometric measurements were performed at current density of -10 mA cm^{-2} . The potentials in this work were converted to a RHE scale according to the Nernst equation ($E_{\text{RHE}} = E_{\text{SCE}} + 0.059 \text{ pH} + 0.245$). All data were presented with iR compensation according to the literature.^[21] The authors obtained the exchange current density from the intercept of the linear region of the Tafel plots.^[11]

Free-Energy Calculations for Atomic Hydrogen Adsorption: The calculations were carried out based on density functional theory and projector augmented wave method as implemented in Vienna ab initio simulation package.^[49] The generalized gradient approximation of Perdew, Burke, and Ernzerhof was employed for the exchange-correlation potential.^[50] The cut-off energy for plane-wave basis sets was set to 400 eV and a self-consistency criterion of 10^{-6} eV was used for the total energy. The structures were relaxed until the residual forces on the atoms had declined to less than 0.01 eV \AA^{-1} . A $6 \times 6 \times 6$ k-mesh was employed for the Brillouin zone integrations.

Supporting Information

Supporting Information is available from the Wiley Online Library or from the author.

Acknowledgements

Research reported in this publication was supported by King Abdullah University of Science and Technology (KAUST). The authors wish to thank the staff of the Imaging and Characterization Laboratory at KAUST, especially Dr. Chao Zhao for his help with the TEM analysis.

Received: September 20, 2016

Revised: November 7, 2016

Published online: January 6, 2017

- [1] L. Liang, H. Cheng, F. Lei, J. Han, S. Gao, C. Wang, Y. Sun, S. Qamar, S. Wei, Y. Xie, *Angew. Chem., Int. Ed.* **2015**, *54*, 12004.
- [2] M. R. Gao, J. X. Liang, Y. R. Zheng, Y. F. Xu, J. Jiang, Q. Gao, J. Li, S. H. Yu, *Nat. Commun.* **2015**, *6*, 5982.
- [3] M. S. Faber, M. A. Lukowski, Q. Ding, N. S. Kaiser, S. Jin, *J. Phys. Chem. C* **2014**, *118*, 21347.
- [4] D. Kong, H. Wang, Z. Lu, Y. Cui, *J. Am. Chem. Soc.* **2014**, *136*, 4897.
- [5] H. Zhang, Y. Li, G. Zhang, P. Wan, T. Xu, X. Wu, X. Sun, *Electrochim. Acta* **2014**, *148*, 170.
- [6] H. Zhang, Y. Li, G. Zhang, T. Xu, P. Wan, X. Sun, *J. Mater. Chem. A* **2015**, *3*, 6306.
- [7] Q. Liu, J. Shi, J. Hu, A. M. Asiri, Y. Luo, X. Sun, *ACS Appl. Mater. Interfaces* **2015**, *7*, 3877.
- [8] D. Y. Wang, M. Gong, H. L. Chou, C. J. Pan, H. A. Chen, Y. Wu, M. C. Lin, M. Guan, J. Yang, C. W. Chen, *J. Am. Chem. Soc.* **2015**, *137*, 1587.
- [9] Y. Liu, X. Hua, C. Xiao, T. Zhou, P. Huang, Z. Guo, B. Pan, Y. Xie, *J. Am. Chem. Soc.* **2016**, *138*, 5087.
- [10] F. Wang, Y. Li, T. A. Shifa, K. Liu, F. Wang, Z. Wang, P. Xu, Q. Wang, J. He, *Angew. Chem.* **2016**, *128*, 7033.
- [11] M. Cabán-Acevedo, M. L. Stone, J. Schmidt, J. G. Thomas, Q. Ding, H. C. Chang, M. L. Tsai, J. H. He, S. Jin, *Nat. Mater.* **2015**, *14*, 1245.
- [12] H. Zhang, B. Yang, X. Wu, Z. Li, L. Lei, X. Zhang, *ACS Appl. Mater. Interfaces* **2015**, *7*, 1772.
- [13] Y. R. Zheng, M. R. Gao, Q. Gao, H. H. Li, J. Xu, Z. Y. Wu, S. H. Yu, *Small* **2015**, *11*, 182.
- [14] Z. Zhang, Y. Liu, L. Ren, H. Zhang, Z. Huang, X. Qi, X. Wei, J. Zhong, *Electrochim. Acta* **2016**, *200*, 142.
- [15] T. Liu, A. M. Asiri, X. Sun, *Nanoscale* **2016**, *8*, 3911.
- [16] C. Xia, Q. Jiang, C. Zhao, M. N. Hedhili, H. N. Alshareef, *Adv. Mater.* **2016**, *28*, 77.
- [17] Q. Gong, L. Cheng, C. Liu, M. Zhang, Q. Feng, H. Ye, M. Zeng, L. Xie, Z. Liu, Y. Li, *ACS Catal.* **2015**, *5*, 2213.
- [18] Y. Liu, H. Cheng, M. Lyu, S. Fan, Q. Liu, W. Zhang, Y. Zhi, C. Wang, C. Xiao, S. Wei, *J. Am. Chem. Soc.* **2014**, *136*, 15670.
- [19] R. Englman, *The Jahn-Teller Effect in Molecules and Crystals*, Wiley-Interscience, New York **1972**.
- [20] H. Liang, F. Meng, M. Cabán-Acevedo, L. Li, A. Forticaux, L. Xiu, Z. Wang, S. Jin, *Nano Lett.* **2015**, *15*, 1421.
- [21] M. S. Faber, R. Dziedzic, M. A. Lukowski, N. S. Kaiser, Q. Ding, S. Jin, *J. Am. Chem. Soc.* **2014**, *136*, 10053.
- [22] H. Yu, X. Yu, Y. Chen, S. Zhang, P. Gao, C. Li, *Nanoscale* **2015**, *7*, 8731.
- [23] B. Qu, X. Yu, Y. Chen, C. Zhu, C. Li, Z. Yin, X. Zhang, *ACS Appl. Mater. Interfaces* **2015**, *7*, 14170.
- [24] F. Yan, C. Zhu, S. Wang, Y. Zhao, X. Zhang, C. Li, Y. Chen, *J. Mater. Chem. A* **2016**, *4*, 6048.
- [25] P. Li, E. Jiang, H. Bai, *J. Phys. D: Appl. Phys.* **2010**, *43*, 265002.
- [26] P. Li, C. Xia, Q. Zhang, Z. Guo, W. Cui, H. Bai, H. N. Alshareef, X. X. Zhang, *J. Appl. Phys.* **2015**, *117*, 223903.
- [27] P. Li, B. Guo, H. Bai, *EPL* **2011**, *94*, 57007.

- [28] W. A. Deer, J. Bowles, R. Howie, D. Vaughan, J. Zussman, *Rock-Forming Minerals: Non-Silicates: Oxides, Hydroxides and Sulphides*, Vol. 5A, Geological Society of London, London **2011**.
- [29] F. Song, X. Hu, *Nat. Commun.* **2014**, 5, 4477.
- [30] J. Xie, S. Li, X. Zhang, J. Zhang, R. Wang, H. Zhang, B. Pan, Y. Xie, *Chem. Sci.* **2014**, 5, 4615.
- [31] G.-Q. Han, Y.-R. Liu, W.-H. Hu, B. Dong, X. Li, Y.-M. Chai, Y.-Q. Liu, C.-G. Liu, *Mater. Chem. Phys.* **2015**, 167, 271.
- [32] J. Kibsgaard, Z. Chen, B. N. Reinecke, T. F. Jaramillo, *Nat. Mater.* **2012**, 11, 963.
- [33] J. Xie, H. Zhang, S. Li, R. Wang, X. Sun, M. Zhou, J. Zhou, X. W. D. Lou, Y. Xie, *Adv. Mater.* **2013**, 25, 5807.
- [34] C. Tsai, F. Abild-Pedersen, J. K. Nørskov, *Nano Lett.* **2014**, 14, 1381.
- [35] Q. Lu, J. Hu, K. Tang, B. Deng, Y. Qian, G. Zhou, X. Liu, *Mater. Chem. Phys.* **2001**, 69, 278.
- [36] W. Zhang, Z. Yang, J. Liu, Z. Hui, W. Yu, Y. Qian, G. Zhou, L. Yang, *Mater. Res. Bull.* **2000**, 35, 2403.
- [37] W. S. Sheldrick, M. Wachhold, *Angew. Chem., Int. Ed. Engl.* **1997**, 36, 206.
- [38] N. Chen, J. H. Zeng, F. Q. Li, W. Q. Zhang, Y. T. Qian, *J. Cryst. Growth* **2002**, 235, 505.
- [39] M. R. Gao, W. T. Yao, H. B. Yao, S. H. Yu, *J. Am. Chem. Soc.* **2009**, 131, 7486.
- [40] Y. Li, H. Liao, Y. Ding, Y. Fan, Y. Zhang, Y. Qian, *Inorg. Chem.* **1999**, 38, 1382.
- [41] J. Tian, Q. Liu, A. M. Asiri, X. Sun, *J. Am. Chem. Soc.* **2014**, 136, 7587.
- [42] H. Liang, H. Shi, D. Zhang, F. Ming, R. Wang, J. Zhuo, Z. Wang, *Chem. Mater.* **2016**, 28, 5587.
- [43] C. Tang, L. Xie, X. Sun, A. M. Asiri, Y. He, *Nanotechnology* **2016**, 27, 20LT02.
- [44] X. Long, G. Li, Z. Wang, H. Zhu, T. Zhang, S. Xiao, W. Guo, S. Yang, *J. Am. Chem. Soc.* **2015**, 137, 11900.
- [45] E. A. Hernández-Pagán, N. M. Vargas-Barbosa, T. Wang, Y. Zhao, E. S. Smotkin, T. E. Mallouk, *Energy Environ. Sci.* **2012**, 5, 7582.
- [46] C. Tang, N. Cheng, Z. Pu, W. Xing, X. Sun, *Angew. Chem., Int. Ed.* **2015**, 54, 9351.
- [47] C. Xia, Q. Jiang, C. Zhao, P. M. Beaujuge, H. N. Alshareef, *Nano Energy* **2016**, 24, 78.
- [48] S. Xiong, J. S. Chen, X. W. Lou, H. C. Zeng, *Adv. Funct. Mater.* **2012**, 22, 861.
- [49] G. Kresse, D. Joubert, *Phys. Rev. B* **1999**, 59, 1758.
- [50] J. P. Perdew, K. Burke, M. Ernzerhof, *Phys. Rev. Lett.* **1996**, 77, 3865.